nature communications

Article

https://doi.org/10.1038/s41467-024-46170-6

Epitaxy of wafer-scale single-crystal MoS_2 monolayer via buffer layer control

Received: 19 July 2023

Accepted: 16 February 2024

Published online: 28 February 2024

Check for updates

Lu Li[1,2], Qinqin Wang[1,2], Fanfan Wu[1,2], Qiaoling Xu[3,4], Jinpeng Tian[1,2], Zhiheng Huang[1,2], Qinghe Wang[5], Xuan Zhao[1,2], Qinghua Zhang[1,2], Qinkai Fan[1,2], Xiuzhen Li[1,2], Yalin Peng[1,2], Yangkun Zhang[1,2], Kunshan Ji[1,2], Aomiao Zhi[1,2], Huacong Sun[1,2], Mingtong Zhu[1,2], Jundong Zhu[1,2], Nianpeng Lu[1,2,3], Ying Lu[1,2], Shuopei Wang[3], Xuedong Bai[1,2,3], Yang Xu[1,2], Wei Yang[1,2], Na Li[3], Dongxia Shi[1,2,3], Lede Xian[3], Kaihui Liu[5], Luojun Du[1,2] ✉ & Guangyu Zhang[1,2,3] ✉

Monolayer molybdenum disulfide (MoS_2), an emergent two-dimensional (2D) semiconductor, holds great promise for transcending the fundamental limits of silicon electronics and continue the downscaling of field-effect transistors. To realize its full potential and high-end applications, controlled synthesis of wafer-scale monolayer MoS_2 single crystals on general commercial substrates is highly desired yet challenging. Here, we demonstrate the successful epitaxial growth of 2-inch single-crystal MoS_2 monolayers on industry-compatible substrates of *c*-plane sapphire by engineering the formation of a specific interfacial reconstructed layer through the S/MoO_3 precursor ratio control. The unidirectional alignment and seamless stitching of MoS_2 domains across the entire wafer are demonstrated through cross-dimensional characterizations ranging from atomic- to centimeter-scale. The epitaxial monolayer MoS_2 single crystal shows good wafer-scale uniformity and state-of-the-art quality, as evidenced from the ~100% phonon circular dichroism, exciton valley polarization of ~70%, room-temperature mobility of ~140 $cm^2v^{-1}s^{-1}$, and on/off ratio of ~10^9. Our work provides a simple strategy to produce wafer-scale single-crystal 2D semiconductors on commercial insulator substrates, paving the way towards the further extension of Moore's law and industrial applications of 2D electronic circuits.

Since the creation of integrated circuits in the 1960s, silicon transistors, following the Moore's law, have been shrinking to boost performance and reduce costs over the past half a century[1]. Today, as conventional silicon transistors enter the sub-10 nm technology node and approach their physical limits, new channel materials are urgently required to further scale transistors and extend Moore's law beyond silicon electronics[2–5]. Two-dimensional (2D) semiconductors with atomic thicknesses and dangling-bond-free flat surface have attracted tremendous interest and possess promising prospects for scaling transistors to the end of roadmap[3,4,6]. The International Roadmap for Devices and Systems (IRDS) has listed 2D semiconductors as the potential channel materials in 2017, and

[1]Beijing National Laboratory for Condensed Matter Physics, Institute of Physics, Chinese Academy of Sciences, 100190 Beijing, China. [2]School of Physical Sciences, University of Chinese Academy of Sciences, 100049 Beijing, China. [3]Songshan Lake Materials Laboratory, Dongguan 523808 Guangdong, China. [4]College of Physics and Electronic Engineering, Center for Computational Sciences, Sichuan Normal University, Chengdu 610068, China. [5]Collaborative Innovation Center of Quantum Matter and School of Physics, Peking University, 100871 Beijing, China. ✉e-mail: luojun.du@iphy.ac.cn; gyzhang@iphy.ac.cn

forecasts that 2D electronic circuits will be commercially available by 2034[5].

Monolayer molybdenum disulfide (MoS_2) has been considered as one of the most promising 2D semiconductor candidates for high performance electronic circuits because of its intrinsic high mobility, excellent gate controllability, high on/off current ratio, ultra-low standby current, small dielectric constant, and good stability[7–14]. Indeed, isolated monolayer MoS_2 devices have been successfully demonstrated to perform well at ultra-scaled lengths down sub-1 nm, which are inconceivable in the framework of traditional silicon with scaling gate length limit of ~12 nm[5,9–11,15,16]. Monolayer MoS_2 transistors have also been identified by Intel as one of three breakthrough technologies to break the scaling limit of silicon. To realize its full potential and high-end industrial applications, it is of utmost importance and a prerequisite to product wafer-scale monolayer MoS_2 single crystals on commercial substrates.

Notably, a general theoretical framework is established recently to guide the growth of wafer-scale single-crystal 2D materials[17,18]. In the light of such guideline that the symmetry group of a substrate should be a subgroup of 2D material, *c*-plane sapphire with C_{3v} symmetry offers an industry-compatible substrate for the epitaxial growth of wafer-scale monolayer MoS_2 single-crystals with point group D_{3h} (C_{3v} plus a mirror-reflection symmetry σ_h)[17–19]. Indeed, wafer-scale single-crystal MoS_2 as well as other transition metal dichalcogenides (TMDs) have been epitaxially grown on sapphire substrates by surface step engineering (e.g., controlling the surface step orientation and height)[19–24]. It is noteworthy that such a step engineering strategy can also be applied to epitaxially grow various 2D materials on other substrates[25–31]. However, specially-designed substrates such as deliberately engineered off-cut angles or annealing at harsh temperatures are typically required for surface step engineering. Meanwhile, recent studies demonstrate that growth conditions (e.g., the S/MoO_3 precursor ratio) can control the interface such as formation of a specific atomically thin interfacial buffer layer and thus also have a strong modulation on the unidirectional domain alignment[26,32–36]. Currently, growth condition controlling is usually coordinated with substrate surface step engineering to achieve the grown of wafer-scale monolayer TMD single-crystals.

Now, a natural question is: can we achieve the epitaxial growth of wafer-scale single-crystal MoS_2 monolayers on industry-compatible *c*-plane sapphire substrates by purely growth condition control without the aid of surface step engineering? In this work, we answer this concern in the affirmative and report the synthesis of 2-inch monolayer MoS_2 single crystals on general *c*-plane sapphire substrates by precisely engineering the formation of a specific buffer layer within the substrate-epilayer gap through the control of S/MoO_3 precursor ratio. The unidirectional alignment and seamless stitching of MoS_2 domains are comprehensively demonstrated via multi-scale characterizations ranging from atomic- to macroscopic-scale. The high quality of as-grown monolayer MoS_2 single crystals is evidenced by the state-of-the-art electron, phonon, and exciton properties, comparable to or even better than that of exfoliated ones. Our results offer a simple strategy to epitaxially grow wafer-scale single-crystal MoS_2 monolayer on commercial insulator substrates and can also been applied to a wide variety of other 2D materials, laying a strong foundation for 2D electronic circuits to fit into industrial settings.

Results

Unidirectional domain alignment by buffer layer control

Figure 1a–c presents the optical micrographs of the as-grown MoS_2 triangular domains on *c*-plane sapphire substrates with a major miscut angle (~0.2°) towards M-axis under three representative MoO_3/S precursor ratios: 3.9% (Fig. 1a), 4.5% (Fig. 1b) and 5.1% (Fig. 1c). Remarkably, the degree of unidirectional alignment strongly depends on the MoO_3/S precursor ratio, which is defined as:

$$\rho = \frac{n_{max} - n_{min}}{n_{max} + n_{min}} \tag{1}$$

where the n_{max} (n_{min}) corresponds to the number of oriented MoS_2 domains in the majority (minority). For 4.5% MoO_3/S precursor ratio, the degree of unidirectional alignment is more than 99%. Note that this value is extracted based on orientation statistics across the entire 2-inch wafer (please see Supplementary Note 1 for microscopy images over a ~1 mm^2 area). By contrast, the degree of unidirectional alignment is essentially zero for 3.9% and 5.1% MoO_3/S precursor ratios. Figure 1g shows the degree of unidirectional alignment against the MoO_3/S precursor ratios. Clearly, the degree of unidirectional alignment can be continuously tuned from ~0 to ~ 100% by controlling the MoO_3/S precursor ratio (please see Supplementary Note 2 for more MoO_3/S precursor ratios). This indicates that pure MoO_3/S precursor ratio control can endow with the unidirectional domain alignment. In addition to *c*-plane sapphire substrates with a major miscut angle (~0.2°) towards M-axis, the unidirectional domain alignment has also been achieved by precisely controlling the S/MoO_3 precursor ratio on pure *c*-plane sapphires, and *c*-plane sapphire substrates with different major miscut angles towards other axes (please see Supplementary Note 3), indicating the universality of our method. It is noteworthy that for all the MoO_3/S ratios we have investigated (ranging from ~3.83% to ~5.55%), it always belongs to a S-rich condition. Consequently, the shape of MoS_2 crystals remains unchanged (please see Supplementary Note 4), in contrast prior work where the drastic changes in S/Mo ratio lead to the shape evolution[37,38].

Upon extending the growth time, the unidirectional oriented MoS_2 domains start to merge and eventually coalesce into a continuous monolayer film at ~45 min (Fig. 1d–f). Figure 1j shows the photograph of the as-grown 2-inch monolayer MoS_2 wafer on *c*-plane sapphire substrates with a major miscut angle towards M axis. Atomic force microscope (AFM) images taken from different locations across a 2-inch wafer manifest a uniform and wrinkle-free monolayer MoS_2 film with a thickness of ~0.7 nm (please see Supplementary Note 5). It is worth stressing that compared to surface engineering techniques employed in previous work that require a special design for the substrate[19–21,25,26], our precursor ratio control strategy holds unique advantages and can fit the *c*-plane sapphire substrates with a major miscut angle (~0.2°) towards M axis, which are mainly supplied on the market and industry-compatible (please see Supplementary Note 6). Although surface steps can also be present in c-plane sapphire substrates with a major miscut angle towards M axis, they are perpendicular to the zigzag edge of triangular MoS_2 domains and therefore have no effect on the unidirectional domain alignment (please see Supplementary Note 7 for details).

To understand the underlying growth mechanism, we perform the cross-sectional high-angle annular dark-field scanning transmission electron microscopy (HAADF-STEM) of the as-grown MoS_2 with unidirectional domain alignment (Fig. 1i). Importantly, an atomically thin buffer layer is observed between the grown MoS_2 layer and the *c*-plane sapphire substrate. By contrast, no buffer layer is formed below the as-grown MoS_2 is observed when the degree of unidirectional alignment is ~0 (Supplementary Fig. 11). This suggests that the buffer layer within the substrate-epilayer gap is the key to facilitate the unidirectional epitaxy of the monolayer MoS_2 and has been recently demonstrated for unidirectional MoS_2 epitaxy on β-Ga_2O_3 (Fig. 1h)[35]. It is noteworthy that for previously reported unidirectional TMDs on sapphire substrates, a buffer layer is also typically observed, but its role is usually ignored[19,20,34].

To further confirm the effect of the buffer layer and its role on unidirectional domain alignment, we remove the as-grown unidirectional MoS_2 from *c*-plane sapphire substrate by water-assisted

technique[39,40]. It is noteworthy that such removal process utilizes the water intercalation and would not destroy the buffer layer. Then the sapphire substrates with buffer layers are used to re-grow MoS_2. Note that we also put fresh sapphire substrates in the growth chamber at the same time for control samples. For fresh sapphire substrates, two antiparallel domains appear simultaneously (please see Supplementary Fig. 12). By contrast, unidirectional MoS_2 domains are reproduced on the sapphire substrates with buffer layers (Supplementary Fig. 12). This result strongly demonstrates the key role of buffer layer on the unidirectional domain alignment. By performing X-ray photoelectron spectroscopy and density functional theory calculation, we infer that one possible configuration of the buffer layer is O–Mo–O–Al, with Mo exhibiting a (+5) oxidation state (Supplementary Note 9).

Seamless stitching of MoS_2 domains

To realize the goal of wafer-scale single-crystal MoS_2 monolayers, seamless stitching of aligned grains must also be satisfied simultaneously, in addition to the unidirectional domain alignment[18,41,42]. To verify the seamless stitching and the absence of grain boundaries, partially merged MoS_2 domains were characterized by atomic-resolution aberration-corrected HAADF-STEM. Figure 2a shows a low-magnification STEM image from the merged area of the two aligned MoS_2 domains. The angle between two merged MoS_2 grains is ~60°. Figure 2b displays six representative atomic-resolution STEM images taken at the corresponding locations marked in Fig. 2a. The identical lattice orientation without grain boundary continuously across the merging zone strongly evidences the seamless stitching of the MoS_2 domains and therefore single-crystal nature. Additionally, the atomic-resolution STEM images show a honeycomb lattice with d-spacing of 0.158 nm and 0.274 nm, corresponding to the $(11\bar{2}0)$ and $(10\bar{1}0)$ planes of monolayer MoS_2, consistent with previous work[43]. More STEM images of merged areas that support the seamless stitching of MoS_2 domains can be found in Supplementary Note 10.

Polarized second-harmonic generation (SHG), which is highly sensitive to grain boundaries[44,45], is further performed to confirm the seamless stitching of MoS_2 domains at the large scale. Figure 2c shows the representative polarized SHG mapping of two unidirectionally merged domains. Uniform signal is observed with no obvious intensity fluctuations across the merging area. This is strongly distinct to the antiparallel domains, where a dark line appears at the grain boundary (Fig. 2e). Figure 2d presents the polarized SHG mapping of a continuous MoS_2 film consisting of unidirectional aligned domains, showing a uniform distribution of intensity over the entire area. This provides a strong proof of the absence of grain boundaries and seamless stitching, in contrast to result of polycrystalline MoS_2 film (Fig. 2f). Besides, etching experiments with hot water vapors are also performed to verify the seamless stitching of unidirectional aligned MoS_2 domains (Supplementary Note 11).

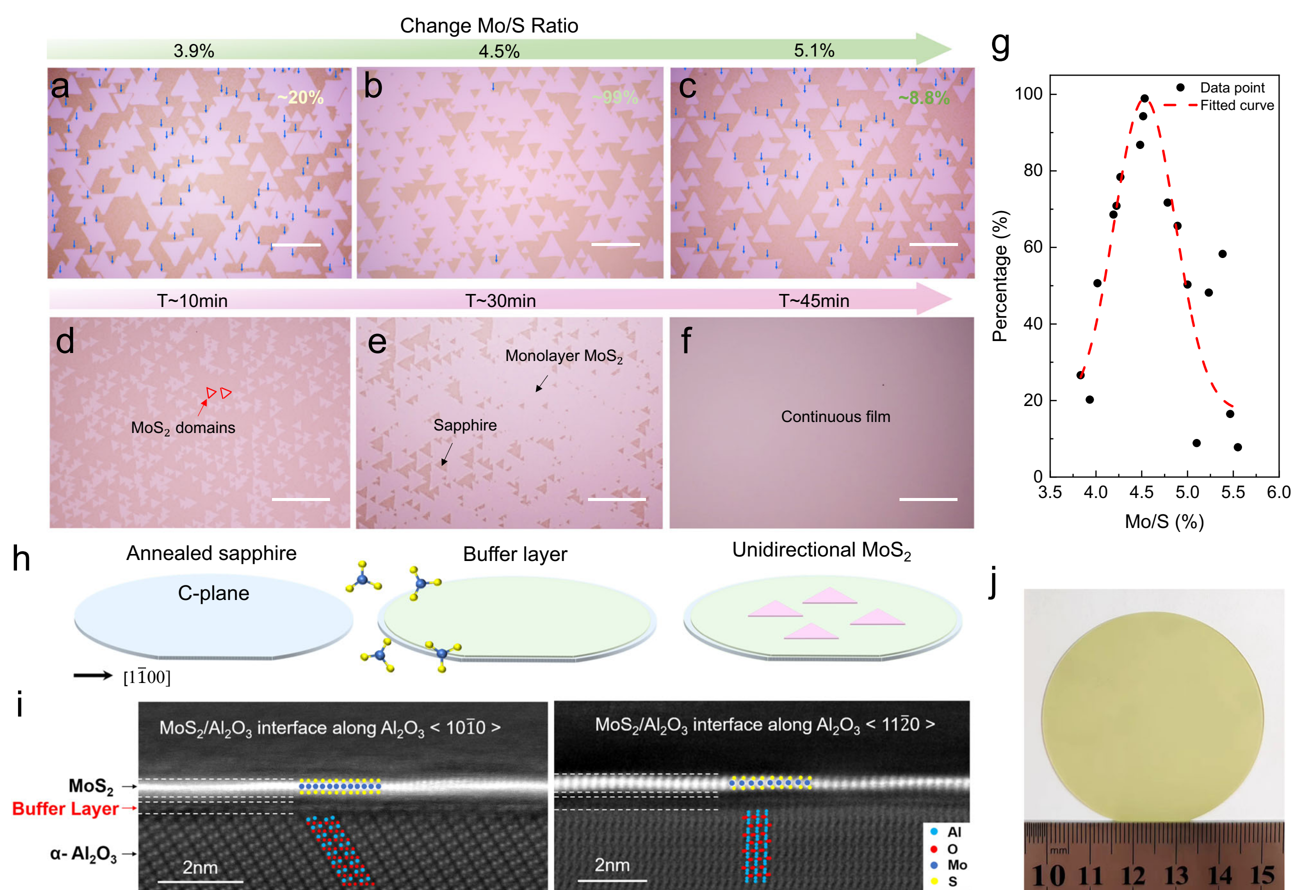

Fig. 1 | Unidirectional domain alignment enabled by buffer layer control. Optical microscopy images of the as-grown MoS_2 triangular domains under three representative MoO_3/S precursor ratios: 3.9% (**a**), 4.5% (**b**) and 5.1% (**c**). Scale bar, 20 μm. Optical micrographs of MoS_2 at different growth stages: nucleation (**d**), stitching (**e**) and coalescence of grains (**f**). Scale bar, 30 μm. **g** The degree of unidirectional alignment as a function of the MoO_3/S precursor ratio. Dashed line is the curve fitted by the Gaussian function. **h** Schematic illustration of the buffer layer control strategy toward the synthesis of wafer-scale monolayer MoS_2 single crystals. **i** Cross-sectional high-angle annular dark-field scanning transmission electron microscopy (HAADF-STEM) images of a MoS_2 grown on the c-plane sapphire substrate along the <10$\bar{1}$0> and <11$\bar{2}$0> directions. **j** Photograph of the as-grown full-coverage monolayer MoS_2 on 2-inch c-plane sapphire substrate with a major miscut angle towards M axis.

https://doi.org/10.1038/s41467-024-46170-6

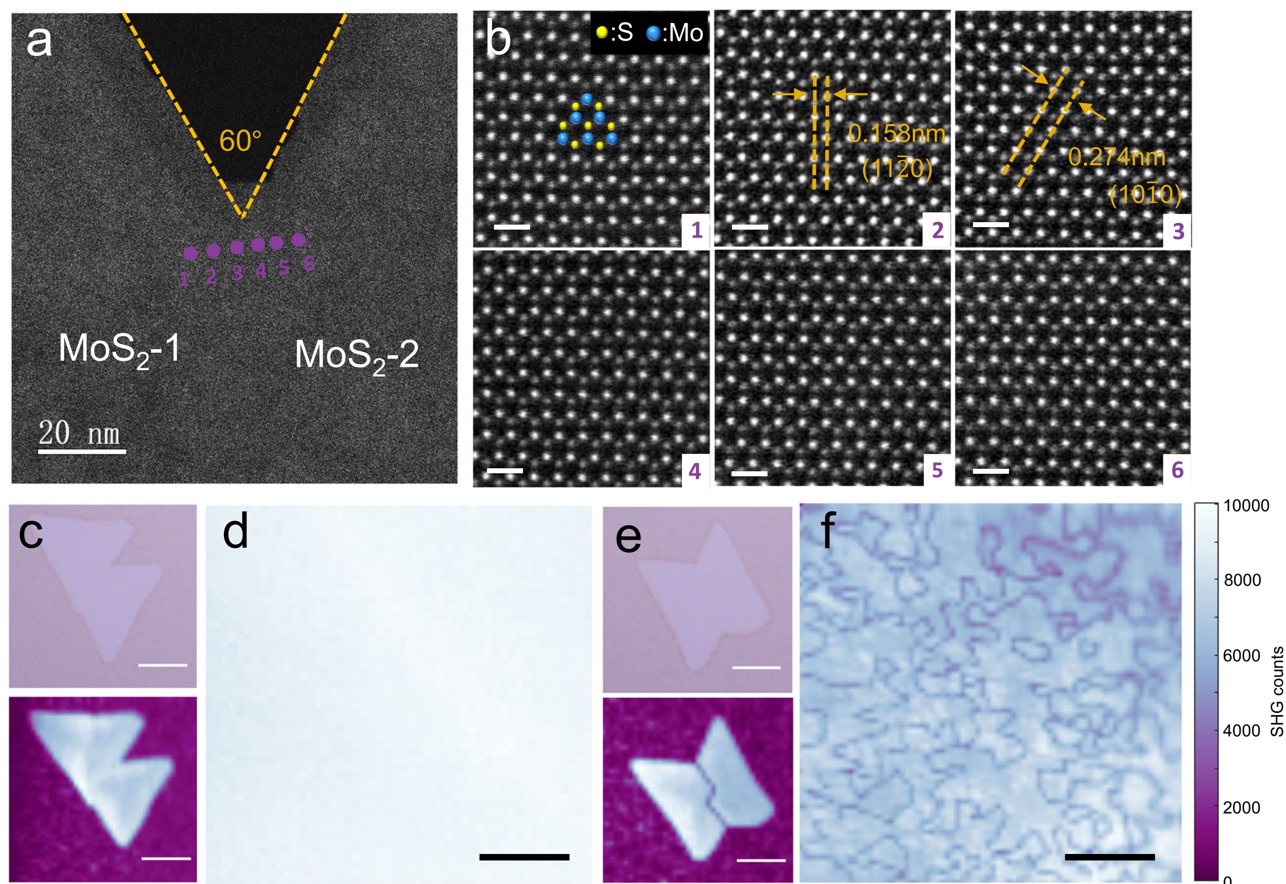

Fig. 2 | Seamless stitching of unidirectional MoS_2 domains. a HAADF-STEM image of the merging area between two unidirectional MoS_2 domains. The orange dashed lines outline the edge of the two aligned MoS_2 domains. **b** 1–6: six typically atomic-resolution HAADF-STEM images obtained from the locations marked in **a**, showing that no boundary was formed, the *d*-spacings of the $(10\bar{1}0)$ and $(11\bar{2}0)$ planes of MoS_2 are 0.274 and 0.158 nm, respectively. Scale bars, 0.5 nm. The atomic-resolution HAADF-STEM images are filtered to enhance the contrast. **c**, **e** Optical microscopy (upper panel) and polarized second-harmonic generation (SHG) mapping (lower panel) of two aligned (**c**) and misaligned (**e**) MoS_2 domains. Scale bars, 5 µm. **d**, **f** Polarized SHG mapping of continuous film formation of single oriented domains (**d**) and misaligned domains (**f**). Scale bars, 20 µm.

Wafer-scale uniformity and high quality

The quality and uniformity of the as-grown single crystal monolayer MoS_2 wafers are illustrated via multi-scale characterizations. Figure 3a presents the low-energy electron diffraction (LEED) patterns measured at twelve random locations across over an area of more than 1 cm^2. The essentially identical LEED patterns provide strong evidences of the uniformity of the as-grown single crystal monolayer MoS_2. In addition, the LEED patterns show three bright diffraction spots, which unambiguously proves the three-fold rotational symmetry and therefore the single-crystalline nature of the as-grown monolayer MoS_2 film (Supplementary Note 12)[21]. Figure 3b is the stacked nine polarization-resolved SHG patterns across a 1 cm^2 sample area (SHG patterns from different locations are indicated by different colors). The nearly overlapped SHG six-petal patterns confirm the coherent lattice orientation and uniformity of the as-grown monolayer MoS_2 film. Figure 3c, d shows 25 representative room-temperature Raman and photoluminescence (PL) spectra across a 2-inch MoS_2 wafer, respectively (please also refer to Raman and PL mapping in Supplementary Note 13). No apparent changes in the peak position and linewidth of both phonons and excitons are observed, illustrating the wafer-scale uniformity. Figure 3e presents a representative fluorescence microscope image of the as-grown monolayer MoS_2. The uniform color contrast confirms the uniformity of the monolayer MoS_2 film. The wafer-scale uniformity of the as-grown monolayer MoS_2 single crystal is also scrutinized by optical micrographs taken at different locations across a 2-inch range (Supplementary Note 14).

The high quality of the grown 2-inch monolayer MoS_2 single crystals is first characterized by aberration-corrected STEM. A statistical analysis of the atomic-resolution images shows that the density of sulfur vacancies in epitaxial monolayer MoS_2 is $\sim 5.2 \times 10^{12} cm^2$ (Supplementary Fig. 16), which is an order of magnitude lower than that of the previously reported exfoliated flakes[46]. The quality of the as-grown single crystal monolayer MoS_2 film was further scrutinized by helicity-resolved inelastic Raman scattering and exciton valley polarization. Figure 3f shows the circular polarization-resolved Raman spectra at room temperature, excited by left-hand σ^+ radiation at 532 nm (2.33 eV). Strikingly, the characteristic in-plane phonon $E^1{}_{2g}$ (out-of-plane vibration A_{1g}) features a strong signal only under cross-circularly (co-circularly) polarized detection, while cannot be detected under the co-circularly (cross-circularly) polarized configuration. This evidences the perfect negative (positive) 100% phonon circular dichroism of $E^1{}_{2g}$ (A_{1g}), as expected for the Raman selection rule determined by the perfect structure of monolayer MoS_2[47], which proves the negligible defect-lattice scattering and high crystal quality. Figure 3g is the non-polarized PL spectrum of the as-grown monolayer MoS_2 at 10 K. The full width at half maximum (FWHM) is ~23 meV, which is only about half of the values in exfoliated flakes[48] (Supplementary Note 15). Figure 3h presents the helicity-resolved PL spectra of the epitaxially grown monolayer MoS_2 at 10 K, excited by σ^+ radiation on resonance with the A exciton at 633 nm (1.96 eV). Remarkably, the degree of exciton

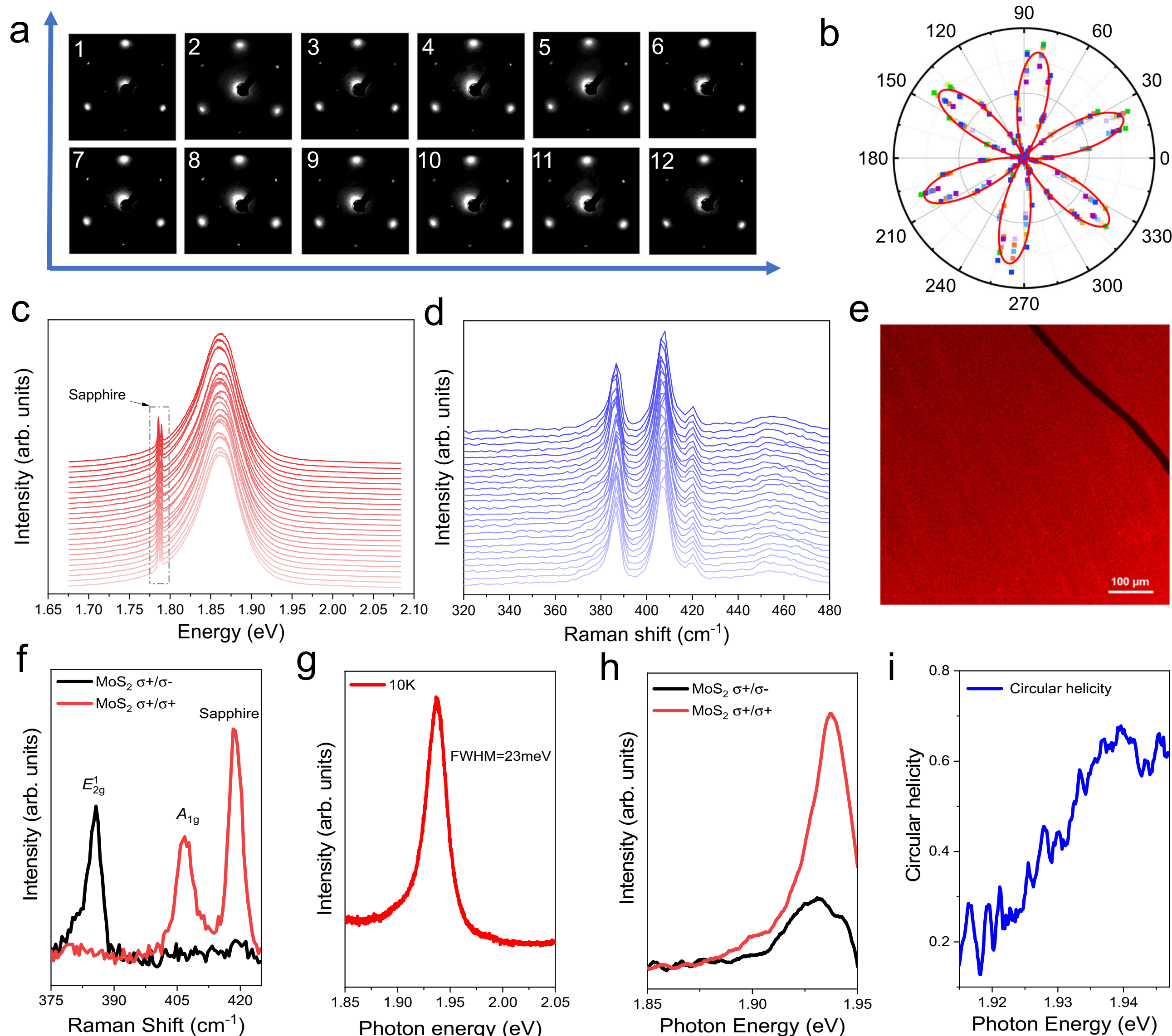

Fig. 3 | Wafer-scale uniformity and high quality. a Representative low-energy electron diffraction (LEED) patterns of a continuous MoS_2 film indicating the single domain orientation nature of the MoS_2 film, taken at 95 eV. **b** Stacked linearly polarized SHG six-petal patterns. SHG from different locations is indicated by symbols with different colors. Solid line is the fitting result to show the six-petal pattern. **c**, **d** Representative photoluminescence (PL) spectra (**c**) and Raman spectra (**d**) at 25 different locations on the wafer. Dash-dotted box highlights the PL signals from sapphire substrate. **e** Fluorescence microscope image of the as-grown film. A scratch has been intentionally created in the upper right corner to endow with a clear contrast between MoS_2 film and bare sapphire substrate. Scale bars, 100 µm. **f** Polarization-resolved Raman spectra for 532 nm excitation. **g** The low-temperature (10 K) PL spectra of the as-grown MoS_2. **h** Circularly polarized PL spectra of the as-grown MoS_2 at 10 K, Excitation light is right-handed circularly polarized (σ^+) at 1.96 eV (633 nm). **i** Circular polarization calculated from the PL spectra in **h**. The high value about 68% indicates the high quality of the MoS_2 film.

valley polarization can reach ~68% (Fig. 3i), which is quantified as:

$$\rho_v = \frac{I(\sigma^+/\sigma^+) - I(\sigma^+/\sigma^-)}{I(\sigma^+/\sigma^+) + I(\sigma^+/\sigma^-)} \tag{2}$$

where $I(\sigma^+/\sigma^+)$ and $I(\sigma^+/\sigma^-)$ denote the exciton emission intensities under the co- and cross-circularly polarized configurations, respectively. Note that the exciton valley polarization of ~ 68% is competitive to or even better than those of the best exfoliated flakes (Supplementary Note 15)[48–50]. Given that exciton valley polarization is highly sensitive to defects as they can introduce intervalley scattering to degrade the circular helicity[48,49], the high exciton valley polarization offers strong evidence for the state-of-the-art quality of our epitaxial monolayer MoS_2 single crystals. The high-quality of the as-grown monolayer MoS_2 single crystals can be understood from several aspects. First, we keep a sulfur-rich condition during the growth, facilitating achieving a low density of sulfur vacancies. Second, our chemical vapor deposition (CVD) setup has a unique multisource design (Supplementary Fig. 27), which facilitates the homogeneous cross-sectional source supply and thus high quality. Besides, our monolayer MoS_2 single crystals are stitched from unidirectional domains on mono-step sapphire surfaces and the nucleation and growth of domains do not rely on the surface steps, thus we believe that the high-quality of as-grown films would also benefit from such good stitching.

The state-of-the-art device performances

The high quality of the as-grown single-crystal monolayer MoS_2, in principle, would enable the superior device performances. To confirm this, we fabricated field-effect transistors (FETs) for performance

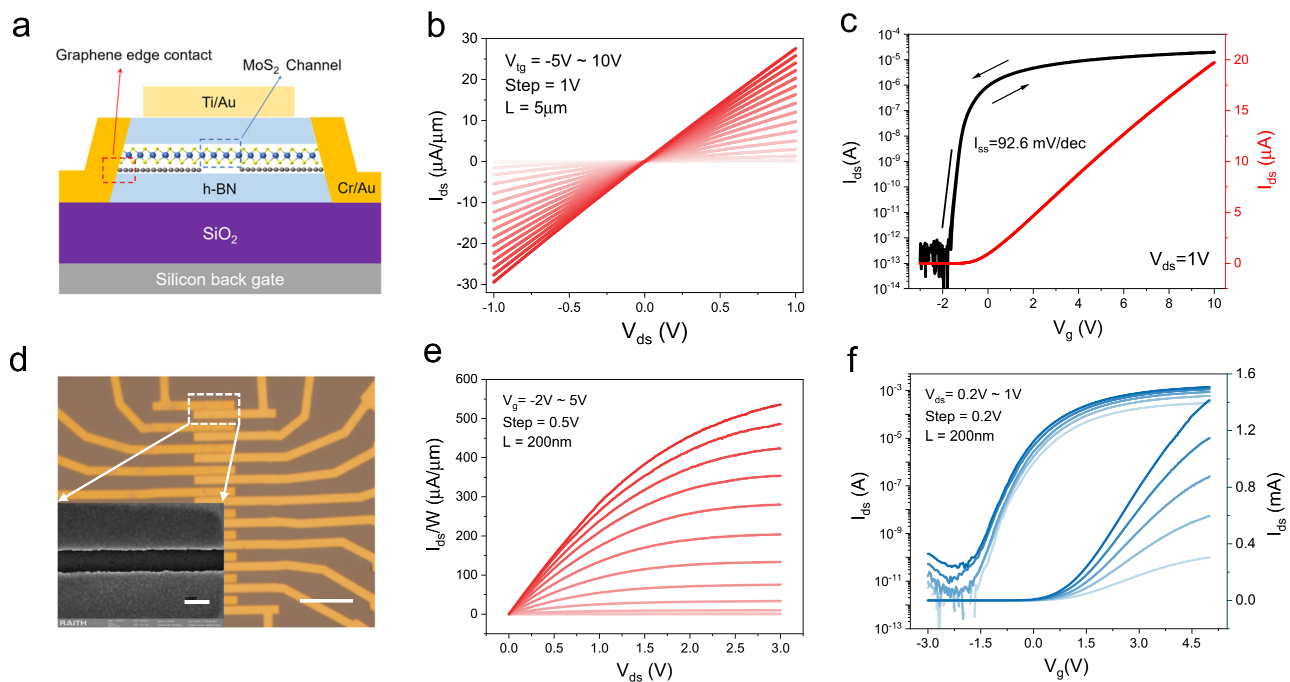

Fig. 4 | The state-of-the-art device performances. **a** Schematic diagram of the typical structure of *h*-BN encapsulated devices. **b**, **c** Output and transfer curves of a *h*-BN encapsulated MoS_2 device with channel length/width (L/W) of 5 µm/1 µm at V_{bg} = 0 V. **d** Photograph of the short channel device. Scale bar, 20 µm. Inset shows the scanning electron microscopy image of the device. Scale bar, 200 nm. **e**, **f** Output and transfer curves of the short channel device with channel length/width (L/W) of 200 nm/5 µm.

benchmark testing. To effectively suppress interfacial scattering and extract intrinsic electronic properties, hexagonal boron nitride (*h*-BN) encapsulated devices based on the epitaxially grown single-crystal monolayer MoS_2 are fabricated utilizing the pick-up technique[51] (see Methods for more details). Figure 4a schematically shows the typical structure of *h*-BN encapsulated devices, with heavily doped silicon (Ti/Au) as the bottom (top) gate. It is noteworthy that monolayer graphene with a narrow electron density distribution around the Fermi level, which can act as a Dirac source and enables the low Schottky barriers[11,52], is adopted as the as source and drain contact electrodes. Figure 4b, c shows the room-temperature output/transfer characteristics of a *h*-BN encapsulated device with channel length/width of 5 µm/1 µm. The thickness of top and bottom *h*-BN layers is ~27 nm and ~34 nm, respectively (Supplementary Fig. 22). Please refer to Supplementary Fig. 24 for the transfer characteristics of more devices. Linear I_{ds}-V_{ds} output characteristic curves (Fig. 4b) indicate the ohmic contact behavior. As can be seen from the transfer characteristic curve (Fig. 4c), the device features an on/off ratio up to ~10^8, negligible electrical hysteresis, and a sharp subthreshold swing of ~92.6 mV/dec across over three orders of magnitude. Remarkably, the extracted field-effect mobility ($\mu = G_m \frac{L}{WC_iV_{ds}}$, where G_m is the transconductance, C_i denotes the gate capacitance, V_{ds} is the source-drain bias, L and W are channel length and width, respectively) can reach ~140 $cm^2s^{-1}V^{-1}$ at room-temperature, which is larger than the results based on polycrystalline films and competitive to highest value of the exfoliated flakes[39,53–55]. For total 10 *h*-BN encapsulated devices from different locations, the average mobility is ~120 $cm^2s^{-1}V^{-1}$. It is noteworthy that the current electron mobility is underestimated and can be further improved by ultra-low/free contact resistance engineering[54,56–58]. Additionally, batch production of uncapsulated FET arrays over several centimeters is achieved based on the as-grown wafer-scale single-crystal MoS_2 monolayer (Supplementary Note 17). Although the uncapsulated FETs show lower mobility than encapsulated ones (which may stem from interfacial scattering and contaminations in the device fabrication processes), a statistical analysis of 150 FETs over an inch scale shows a high yield >97% and an average on/off ratio of devices of ~10^8 (Supplementary Note 17). Finally, 200 nm short-channel FET devices based on the as-grown monolayer MoS_2 were fabricated, as shown in Fig. 4d. Figure 4e, f shows the electrical output and transfer characteristic curves of the short-channel device, respectively. The short-channel device exhibits a saturation on-current density of ~535 µA/µm, a high on/off ratio close to 10^9 and a sharp subthreshold swing of 107 mV/dec. The overall device performances of our wafer-scale single-crystal MoS_2 monolayers (e.g., mobility of 140 $cm^2s^{-1}V^{-1}$, on-current density of ~535 µA/µm and 10^9 on/off ratio) are quite competitive to those best results among all the monolayer TMDC transistors reported so far (Supplementary Table 1), holding promising prospects for large-scale integrated applications.

Discussion

In conclusion, we demonstrate a simple strategy of precursor ratio control for the batch production of wafer-scale single-crystal MoS_2 monolayer films on industry-compatible substrates of *c*-plane sapphire. The epitaxial monolayer MoS_2 single crystals exhibit wafer-scale uniformity and the state-of-the-art properties, evidenced by the perfect phonon circular dichroism, exciton valley polarization of ~70%, room-temperature mobility of ~140 $cm^2v^{-1}s^{-1}$, on-current density of ~535 µA/µm, and a nearly 10^9 on/off ratio. Our work offers a novel insight into the synthesis of wafer-scale high-quality 2D semiconductors and lays a solid foundation for industrial applications of 2D integrated electronic circuits.

Methods

Growth of single-crystal MoS_2 monolayers on *c*-plane sapphire

The growth of single crystalline monolayer MoS_2 was carried out in a three-temperature zone CVD system with multisource design manufactured by Dongguan Join Technology Co., Ltd (please refer to Supplementary Figs. 27 and 28 for the schematic diagram and photographs of our CVD setup, repectively). For a typical growth, the center mini-tube is loaded with sulfur (Alfa Aesar, 99.9%, 6 g) and

flowed with 40 sccm Ar. Note that to effectively load sulfur, a large rectangular chamber is designed ~5 cm from the end of the quartz tube. The surface area of melted sulfur determined by the rectangular chamber is around 25 cm^2. For the outside six mini-tubes, every-other-tube is loaded with MoO_3 (Alfa Aesar, 99.999%) and flowed with Ar/O_2 (40/0.5 sccm); and the other three empty tubes are also flowed with Ar/O_2 (40/0.5 sccm). In addition, to avoid the powder being blown away by the carrier gas, we use MoO_3 thin flack (the thickness is ~0.5 mm) which is obtained by pressing the MoO_3 powder (Alfa Aesar, 99.999%) with a hydraulic press. All the quartz tubes have an inner diameter of ~1 cm. The distance between MoO_3 and substrate (sulfur) is ~32 cm–40 cm (~17 cm). During the growth, sulfur, MoO_3 and sapphire substrate are placed at first, second, and third temperature zones, respectively. The temperatures for the sulfur, MoO_3, and sapphire substrate are 120, 560, and 880 °C, respectively. The pressure is kept at about 1 torr during the growth process. The growth time ranged from 15 mins (to obtain single oriented discrete MoS_2 domains) to 45 mins (to obtain single oriented continuous MoS_2 films), and the pressure was kept at about 1 torr during the growth process, and the LPCVD system was cooled to room temperature in the argon gas stream after the growth.

AFM imaging was performed by Asylum Research Cypher S. The thickness of the grown MoS_2 film is measured by scraping the film at the wafer corner. LEED measurements were performed in vacuum environments ($<3 \times 10^{-7}$ Pa) using the Omicron LEED system. A high-resolution four-circle X-ray diffractometer (Smartlab, Rigaku) was used to characterize the in-plane crystalline symmetry of the grown wafer-scale MoS_2 film.

Optical characterizations

SHG microscopy measurements was performed in a homemade system. A femtosecond laser with 780 nm central wavelength (~100 fs, 100 MHz, generated by MenloSystems) and power of 1.8 mW was used to excite the sample. The laser beam passes through a linear polarizer and was tightly focused to ~1 μm spot diameter by a 100× objective (NA = 0.9, Nikon). The MoS_2 samples were attached to a piezoelectric stage to realize sub-micrometer scanning. The SHG signals were collected by the same objective, then passed through another linear polarizer whose polarization angle is perpendicular to the excitation beam. A band pass filter was used to filter out the 780 nm fundamental beam. The SHG intensities were measured by a spectrometer (Princeton Instrument) with an exposure time of 0.3 s each pixel of the mapping.

Both Raman and PL spectra were collected using a HORIBA spectrometer (LabRAM HR Evolution) in a confocal backscattering configuration. For room-temperature Raman spectra, off-resonance light from 532 nm (2.33 eV) continuous laser with a power of about 900 μw was focused through a Nikon objective (N.A. = 0.5 W.D. = 10.6 F.N. = 26.5) onto the sample with a spot diameter of ~1.5 μm. For PL spectra, on-resonance light from 633 nm (2.33 eV) continuous laser with a power of about 400 μw was focused through the same Nikon objective onto the sample with a spot diameter of ~1 μm. The sample was placed in an optical chamber with a high vacuum and then cooled down to 10 K by a closed cryocooler (CS-204PF-DMX-20B-OM from ARS) for cryogenic PL measurements.

TEM characterizations

The MoS_2 samples for TEM characterizations were prepared by transferring MoS_2 onto the TEM grids (Zhongjingkeyi) using the polymethyl-methacrylate-based transfer method. STEM was performed by an aberration-corrected JEM ARM200F (JEOL) at 200 kV and an aberration-corrected JEOL Grand ARM 300 CFEG operated 80 kV. The SAED was performed with a TEM (Philips CM200) operating at 200 kV.

Transfer of MoS_2 films

Propylene carbonate (PC, Chloroform solution of 6% propylene carbonate) was used to pick up boron nitride (*h*-BN) that has been mechanically exfoliated onto silicon oxide. The picked *h*-BN was dropped onto the as-grown MoS_2 to pick up the single crystal MoS_2. Then, two parallel graphene samples were picked up as contact electrodes. Finally, the sample falls onto bulk *h*-BN on 300-nm silicon oxide substrate to obtain van der Waals heterojunction with clean interface and free of organic residues.

FET fabrication and electrical measurements

Fabrication of *h*-BN encapsulated devices. *h*-BN/MoS_2/Graphene/*h*-BN/SiO_2 samples were fabricated via a propylene-carbonate-based transfer method. Ti(2 nm)/Au(30 nm) metal electrodes were deposited as the top gate of the device using electron beam lithography (EBL), electron beam evaporation and lift-off techniques. EBL was used to reverse expose the Hall shape of the device, and reactive ion etching (RIE, Plasma Lab 80 Plus, Oxford Instruments) was used to etch off the excess *h*-BN/MoS_2/Graphene/*h*-BN to avoid the conduction between the device electrodes. Finally, the device was completed by depositing Cr (3 nm)/Au(30 nm) using an electron beam evaporation system to form a one-dimensional contact with graphene.

Batch fabrication of devices. The patterned Ti (2 nm)/Au (10 nm) metal layer were deposited on sapphire substrate as gate electrodes by UV lithography (MA6, Karl Suss) and electron beam evaporation system, followed by deposition of 20 nm HfO_2 as the dielectric layer by atomic layer deposition (ALD). The as-grown single-crystal MoS_2 was transferred onto HfO_2/Au/Ti/sapphire substrate and then patterned into channels by UV lithography and RIE. The source-drain electrodes are Au/Ti/Au (2/2/10 nm), which are defined by UV lithography, electron beam evaporation and lift-off processes.

Fabrication of short channel devices. The as-grown single-crystal MoS_2 was transferred to a HfO_2 (5 nm)/Si substrate, and the dielectric layer was deposited by ALD. EBL and RIE were then used to defined the channel and drain-source, and Au/Ti/Au (2/2/10 nm) were deposited as drain-source electrodes.

Electrical measurements were carried out with an Agilent B1500 semiconductor parameter analyzer in a four-probe vacuum station with a bass pressure of $\sim 10^{-6}$ mbar at room temperature.

Data availability

Relevant data supporting the key findings of this study are available within the article and the Supplementary Information file. All raw data generated during the current study are available from the corresponding authors upon request.

References

1. Waldrop, M. M. The chips are down for Moore's law. *Nature* **530**, 144–147 (2016).
2. Li, M.-Y., Su, S.-K., Wong, H.-S. P. & Li, L.-J. How 2D semiconductors could extend Moore's law. *Nature* **567**, 169–170 (2019).
3. Liu, Y. et al. Promises and prospects of two-dimensional transistors. *Nature* **591**, 43–53 (2021).
4. Chhowalla, M., Jena, D. & Zhang, H. Two-dimensional semiconductors for transistors. *Nat. Rev. Mater.* **1**, 16052 (2016).
5. IEEE International Roadmap for Devices and Systems. https://irds.ieee.org/editions (2022).
6. Fiori, G. et al. Electronics based on two-dimensional materials. *Nat. Nanotechnol.* **9**, 768–779 (2014).
7. Radisavljevic, B., Radenovic, A., Brivio, J., Giacometti, V. & Kis, A. Single-layer MoS_2 transistors. *Nat. Nanotechnol.* **6**, 147–150 (2011).
8. Migliato Marega, G. et al. Logic-in-memory based on an atomically thin semiconductor. *Nature* **587**, 72–77 (2020).
9. Desai, S. B. et al. MoS_2 transistors with 1-nanometer gate lengths. *Science* **354**, 99–102 (2016).

10. Wu, F. et al. Vertical MoS_2 transistors with sub-1-nm gate lengths. *Nature* **603**, 259–264 (2022).
11. Tian, J. et al. Scaling of MoS_2 Transistors and Inverters to Sub-10 nm Channel Length with High Performance. *Nano Lett.* **23**, 2764 (2023).
12. Li, N. et al. Large-scale flexible and transparent electronics based on monolayer molybdenum disulfide field-effect transistors. *Nat. Electron.* **3**, 711–717 (2020).
13. Tang, J. et al. Low power flexible monolayer MoS_2 integrated circuits. *Nat. Commun.* **14**, 3633 (2023).
14. Wang, Q. et al. Layer-by-layer epitaxy of multi-layer MoS_2 wafers. *Natl Sci. Rev.* **9**, nwac077 (2022).
15. Xie, L. et al. Graphene-Contacted Ultrashort Channel Monolayer MoS_2 Transistors. *Adv. Mater.* **29**, 1702522 (2017).
16. Nourbakhsh, A. et al. MoS_2 Field-Effect Transistor with Sub-10 nm Channel Length. *Nano Lett.* **16**, 7798–7806 (2016).
17. Dong, J., Zhang, L., Dai, X. & Ding, F. The epitaxy of 2D materials growth. *Nat. Commun.* **11**, 5862 (2020).
18. Zhang, L., Dong, J. & Ding, F. Strategies, Status, and Challenges in Wafer Scale Single Crystalline Two-Dimensional Materials Synthesis. *Chem. Rev.* **121**, 6321 (2021).
19. Fu, J.-H. et al. Oriented lateral growth of two-dimensional materials on c-plane sapphire. *Nat. Nanotechnol.* **18**, 1289–1294 (2023).
20. Li, T. et al. Epitaxial growth of wafer-scale molybdenum disulfide semiconductor single crystals on sapphire. *Nat. Nanotechnol.* **16**, 1201–1207 (2021).
21. Wang, J. et al. Dual-coupling-guided epitaxial growth of wafer-scale single-crystal WS_2 monolayer on vicinal a-plane sapphire. *Nat. Nanotechnol.* **17**, 33–38 (2022).
22. Liu, L. et al. Uniform nucleation and epitaxy of bilayer molybdenum disulfide on sapphire. *Nature* **605**, 69–75 (2022).
23. Zheng, P. et al. Universal epitaxy of non-centrosymmetric two-dimensional single-crystal metal dichalcogenides. *Nat. Commun.* **14**, 592 (2023).
24. Li, T. et al. Halide vapor phase epitaxy of monolayer molybdenum diselenide single crystals. *Natl Sci. Open* **2**, 20220055 (2023).
25. Choi, S. H. et al. Epitaxial Single-Crystal Growth of Transition Metal Dichalcogenide Monolayers via the Atomic Sawtooth Au Surface. *Adv. Mater.* **33**, 2006601 (2021).
26. Yang, P. et al. Epitaxial Growth of Centimeter-Scale Single-Crystal MoS_2 Monolayer on Au(111). *ACS Nano* **14**, 5036–5045 (2020).
27. Wang, L. et al. Epitaxial growth of a 100-square-centimetre single-crystal hexagonal boron nitride monolayer on copper. *Nature* **570**, 91–95 (2019).
28. Chen, T.-A. et al. Wafer-scale single-crystal hexagonal boron nitride monolayers on Cu (111). *Nature* **579**, 219–223 (2020).
29. Ma, K. Y. et al. Epitaxial single-crystal hexagonal boron nitride multilayers on Ni (111). *Nature* **606**, 88–93 (2022).
30. Li, J. et al. Single-Crystal MoS_2 Monolayer Wafer Grown on Au (111) Film Substrates. *Small* **17**, 2100743 (2021).
31. Xia, Y. et al. Wafer-scale single-crystalline $MoSe_2$ and WSe_2 monolayers grown by molecular-beam epitaxy at low-temperature-the role of island-substrate interaction and surface steps. *Nat. Sci.* **3**, 20220059 (2023).
32. Aljarb, A. et al. Substrate Lattice-Guided Seed Formation Controls the Orientation of 2D Transition-Metal Dichalcogenides. *ACS Nano* **11**, 9215–9222 (2017).
33. Fu, D. et al. Molecular Beam Epitaxy of Highly Crystalline Monolayer Molybdenum Disulfide on Hexagonal Boron Nitride. *J. Am. Chem. Soc.* **139**, 9392–9400 (2017).
34. Zhu, H. et al. Step engineering for nucleation and domain orientation control in WSe_2 epitaxy on c-plane sapphire. *Nat. Nanotechnol.* **18**, 1295–1302 (2023).
35. Aljarb, A. et al. Interfacial Reconstructed Layer Controls the Orientation of Monolayer Transition-Metal Dichalcogenides. *ACS Nano* **17**, 10010–10018 (2023).
36. Yang, P. et al. Highly Reproducible Epitaxial Growth of Wafer-Scale Single-Crystal Monolayer MoS_2 on Sapphire. *Small Methods* **7**, 2300165 (2023).
37. Wang, S. et al. Shape Evolution of Monolayer MoS_2 Crystals Grown by Chemical Vapor Deposition. *Chem. Mater.* **26**, 6371–6379 (2014).
38. Yang, S. Y., Shim, G. W., Seo, S.-B. & Choi, S.-Y. Effective shape-controlled growth of monolayer MoS_2 flakes by powder-based chemical vapor deposition. *Nano Res.* **10**, 255–262 (2017).
39. Yu, H. et al. Wafer-Scale Growth and Transfer of Highly-Oriented Monolayer MoS_2 Continuous Films. *ACS Nano* **11**, 12001–12007 (2017).
40. Liao, M. et al. Precise control of the interlayer twist angle in large scale MoS_2 homostructures. *Nat. Commun.* **11**, 2153 (2020).
41. Wan, Y. et al. Wafer-scale single-orientation 2D layers by atomic edge-guided epitaxial growth. *Chem. Soc. Rev.* **51**, 803–811 (2022).
42. Chubarov, M. et al. Wafer-Scale Epitaxial Growth of Unidirectional WS_2 Monolayers on Sapphire. *ACS Nano* **15**, 2532–2541 (2021).
43. Lin, Y.-C. et al. Wafer-scale MoS2 thin layers prepared by MoO_3 sulfurization. *Nanoscale* **4**, 6637–6641 (2012).
44. Yin, X. et al. Edge Nonlinear Optics on a MoS_2 Atomic Monolayer. *Science* **344**, 488–490 (2014).
45. Karvonen, L. et al. Rapid visualization of grain boundaries in monolayer MoS_2 by multiphoton microscopy. *Nat. Commun.* **8**, 15714 (2017).
46. Hong, J. et al. Exploring atomic defects in molybdenum disulphide monolayers. *Nat. Commun.* **6**, 6293 (2015).
47. Zhao, Y., Xu, B., Tong, L. & Zhang, J. The helicity of Raman scattered light: principles and applications in two-dimensional materials. *Sci. China Chem.* **65**, 269–283 (2022).
48. Du, L. et al. Robust spin-valley polarization in commensurate MoS_2/graphene heterostructures. *Phys. Rev. B* **97**, 115445 (2018).
49. Zeng, H., Dai, J., Yao, W., Xiao, D. & Cui, X. Valley polarization in MoS_2 monolayers by optical pumping. *Nat. Nanotechnol.* **7**, 490–493 (2012).
50. Suzuki, R. et al. Valley-dependent spin polarization in bulk MoS_2 with broken inversion symmetry. *Nat. Nanotechnol.* **9**, 611–617 (2014).
51. Wu, F. et al. Coupled Ferroelectricity and Correlated States in a Twisted Quadrilayer MoS_2 Moiré Superlattice. *Chin. Phys. Lett.* **40**, 047303 (2023).
52. Liu, Y. et al. Toward Barrier Free Contact to Molybdenum Disulfide Using Graphene Electrodes. *Nano Lett.* **15**, 3030–3034 (2015).
53. Kang, K. et al. High-mobility three-atom-thick semiconducting films with wafer-scale homogeneity. *Nature* **520**, 656–660 (2015).
54. Wang, Y. et al. Van der Waals contacts between three-dimensional metals and two-dimensional semiconductors. *Nature* **568**, 70–74 (2019).
55. Smets, Q. et al. Ultra-scaled MOCVD MoS2 MOSFETs with 42 nm contact pitch and 250 μA/μm drain current. In *International Electron Devices Meeting (IEDM)* 23.2.1–23.2.4 (IEEE, 2019).
56. Liu, Y. et al. Approaching the Schottky–Mott limit in van der Waals metal–semiconductor junctions. *Nature* **557**, 696–700 (2018).
57. Shen, P.-C. et al. Ultralow contact resistance between semimetal and monolayer semiconductors. *Nature* **593**, 211–217 (2021).
58. Li, W. et al. Approaching the quantum limit in two-dimensional semiconductor contacts. *Nature* **613**, 274–279 (2023).

Acknowledgements

We thank Yi Wan for valuable discussions. This work is supported by the National Key Research and Development Program of China (Nos. 2021YFA1202900, 2021YFA1400502, 2021YFA1401300, 2023YFA1407000, 2022YFA1402503), the Key-Area Research and Development Program of Guangdong Province, China (Grant No. 2020B0101340001), Guangdong Major Project of Basic and Applied Basic Research (2021B0301030002), the National Science Foundation

of China (NSFC) under Grant Nos. 61888102, 12274447, 12074412 and 62204166, the Strategic Priority Research Program of Chinese Academy of Sciences (CAS) under Grant No. XDB0470101.

Author contributions

G.Z. and L.D. designed the research; L.L. performed the growth, high-resolution AFM imaging, TEM, spectroscopic characterizations, device fabrication, and electrical transport measurements with help from Q.W. and Y.Z.; F.W. and J.Z. fabricated the h-BN encapsulated devices; J.T. and X.L. fabricated the short-channel devices; Y.P. fabricated batch devices; Z.H. and K.J. performed the cryogenic PL measurements; Q.H.W. and K.L. performed LEED; Q.Z., A.Z., H.S. and X.B. performed TEM; X.Z. and Y.X. performed SHG; M.Z. and N.P.L. performed XRD; Q.F. and Y.L. performed fluorescence microscope imaging; Q.X. and L.X. performed the theoretical calculations; L.L., Y.Z., W.Y., D.S., S.W., N.L. L.D., and G.Z. analyzed data; L.L., L.D., and G.Z wrote and all authors commented on the manuscript.

Competing interests

The authors declare no competing interests.

Additional information

Supplementary information The online version contains supplementary material available at https://doi.org/10.1038/s41467-024-46170-6.

Correspondence and requests for materials should be addressed to Luojun Du or Guangyu Zhang.

Peer review information *Nature Communications* thanks Taotao Li, Ang-Yu Lu and the other, anonymous, reviewer for their contribution to the peer review of this work. A peer review file is available.

Reprints and permissions information is available at http://www.nature.com/reprints

Publisher's note Springer Nature remains neutral with regard to jurisdictional claims in published maps and institutional affiliations.

Open Access This article is licensed under a Creative Commons Attribution 4.0 International License, which permits use, sharing, adaptation, distribution and reproduction in any medium or format, as long as you give appropriate credit to the original author(s) and the source, provide a link to the Creative Commons licence, and indicate if changes were made. The images or other third party material in this article are included in the article's Creative Commons licence, unless indicated otherwise in a credit line to the material. If material is not included in the article's Creative Commons licence and your intended use is not permitted by statutory regulation or exceeds the permitted use, you will need to obtain permission directly from the copyright holder. To view a copy of this licence, visit http://creativecommons.org/licenses/by/4.0/.

© The Author(s) 2024